

A Finite Volume scheme for the solution of discontinuous magnetic field distributions on non-orthogonal meshes

Augusto Riedinger^a, Martín Saravia^{a,*}, José Ramírez^a

^a*Centro de Investigación en Mecánica Teórica y Aplicada, Universidad Tecnológica Nacional, Facultad Regional Bahía Blanca, CONICET. 11 de Abril 461, Bahía Blanca, Argentina.*

Abstract

We present a Finite Volume formulation for determining discontinuous distributions of magnetic fields within non-orthogonal and non-uniform meshes. The numerical approach is based on the discretization of the vector potential variant of the equations governing static magnetic field distribution in magnetized, permeable and current carrying media. After outlining the derivation of the magnetostatic balance equations and its associated boundary conditions, we propose a cell-centered Finite Volume framework for spatial discretization and a Block Gauss–Seidel multi-region scheme for solution. We discuss the structure of the solver, emphasizing its effectiveness and addressing stabilization and correction techniques to enhance computational robustness. We validate the accuracy and efficacy of the approach through numerical experiments and comparisons with the Finite Element method.

Keywords: magnetostatics, Finite Volume Method, Maxwell's equations, OpenFOAM, curved surfaces

*Corresponding author

Email address: msaravia@conicet.gov.ar (José Ramírez)

1. Introduction

Magnetic fields have captivated researchers since their discovery, and in recent years, there has been a surge in their engineering and industrial applications. Consequently, the field of magnetostatics has experienced significant advancements. However, addressing the intricate geometries encountered in real-world applications has always been a major challenge due to the inherent complexity of Maxwell's equations—the fundamental partial differential equations governing the dynamics of magnetic fields [1]. Thus, the application of numerical methods for predicting magnetic fields has become indispensable in tackling this intricate problem and seeking practical solutions.^x

One of the primary consequences of the technological advances in fabrication techniques is the emergence of designs with complex geometries. Although they have proven to enhance the efficiency and appearance of modern devices, the computational simulation of the physical phenomena in which they play a role has become increasingly challenging.

In the landscape of Computational Electromagnetics (CEM), researchers have made remarkable strides since its inception [2, 3, 4]. Pioneering work by T. K. Sarkar et al. laid the groundwork for numerical schemes aimed at solving linear matrix equations, particularly in the context of electromagnetic scattering and radiation problems. Building upon these foundations, subsequent years have witnessed a surge in advancements, as evidenced by the seminal contributions of Salon et al [5]. Further enriching the field, applied investigations have delved into diverse areas, with notable reviews such as Niu et al.'s comprehensive exploration of electromagnetic modeling providing valuable insights [6]. Despite these advancements, the literature addressing the numerical modeling of electromagnetic fields on complex geometries remains relatively sparse.

The Finite Element Method (FEM) has traditionally been employed to numerically solve electromagnetic problems [7]. Early formulations were pioneered by J. H. Coggon et al. [8] and Sadiku [9, 10], who provided a foundational introduction to the FEM applied to electromagnetics. Subsequent advances were made by J. Jin et al. [11] and A. C. Polycarpou et al. [12]. A recent review addressing the use of the FEM to model electromagnetic problems was presented by M. Augustyniak et al. [13].

In contrast, the application of the Finite Volume Method (FVM) to electromagnetics took more time to develop. It began with C.-D. Munz et al. [14], who developed a time domain approach to solve Maxwell equations, later extended by T. S. Chung et al. [15] to general 3D polyhedral domains with discontinuous physical coefficients. Later, Y. Liu et al. [16] investigated spectral FVM on unstructured grids, presenting a method computationally more effective than the conventional structured methods. In parallel, several applied studies emerged, such as the solution of automotive electromagnetic compatibility problems using a hybrid finite difference/Finite Volume method by X. Ferrieres et al. [17], and techniques developed by E. Haber et al. [18] and L. A. C. Mata et al. [19] to reduce the computational cost of solving the Maxwell equations at low frequencies, with direct applications to geophysical settings. However, the aforementioned papers encounter limitations in handling highly non-orthogonal grids and discontinuous magnetic properties across interfaces in domains composed of media of different physical characteristics.

In 2021, Saravia [20] introduced a FVM framework to solve discontinuous distributions of magnetic fields, employing a multi-region approach implemented within the OpenFOAM library. The author presented a formulation written in terms of the magnetic vector potential to determine the distribution of magnetic fields in interacting permeable, permanently magnetized and current carrying media. They benchmarked the accuracy of the FVM multi-region magnetostatic approach against the FEM. Subsequently, Riedinger et al. [21] expanded the framework for single-region schemes, demonstrating that the magnetic field could be accurately captured with a continuous method using boundary layer meshing. Although the mentioned methods have proven to be effective to solve magnetostatic problems, they have not been tested in non-orthogonal meshes.

The literature concerning the numerical treatment of discontinuous distributions of magnetic fields

using the Finite Volume Method is sparse. In particular, the application of this method to obtain solutions to Maxwell's equations on non orthogonal meshes is even scarcer. Nevertheless, the numerous instances of FVM application in other areas of physics which involve complex geometries and non-orthogonal meshes, such as fluid mechanics and heat transfer, suggest that the FVM may still be an appealing option.

In this context, we present a Finite Volume formulation tailored to analyze discontinuous distributions of magnetic fields within non-orthogonal and non-uniform meshes. Our numerical approach centers on discretizing the vector potential variant of the equation governing static magnetic field distribution in magnetized, permeable, and current-carrying media. We provide an overview of the derivation of the magnetostatic balance equations and their associated boundary conditions. Subsequently, we introduce a cell-centered Finite Volume framework for spatial discretization and propose a Block Gauss-Seidel multi-region scheme for solution. Emphasizing the structure of the solver, we highlight its effectiveness and discuss stabilization and limiting techniques aimed at enhancing computational robustness. Through numerical experiments and comparisons with the Finite Element Method, we validate the accuracy and efficacy of the formulation.

2. Magnetostatic formulation

2.1. Conservation laws

We begin assuming that currents are not changing with time. Then, Maxwell's equations may be separated into two sets: one for the electric field and another for the magnetic field. Under this conditions, magnetic fields are static, and the conservation laws reduce to

$$\nabla \cdot \mathbf{B} = 0 \quad (1)$$

and

$$\nabla \times \mathbf{B} = \mu_0 \mathbf{J}_f \quad (2)$$

for the magnetic field \mathbf{B} , and

$$\nabla \cdot \mathbf{J}_f = 0 \quad (3)$$

for the free current \mathbf{J}_f [22, 23]. Equation (1) is Gauss' law for magnetism and (2) is Ampere's law.

The numerical solution to these equations within the context of permeable, magnetized, and current-carrying media necessitates formulating equilibrium equations and associated boundary conditions governing the behavior of the magnetic field. In the subsequent sections, we outline the derivation process.

2.2. Ampere's law

2.2.1. Permeable media and current carrying media

The distribution of the magnetic fields within a permeable domain is governed by a variant of Ampere's law given by

$$\nabla \times \mathbf{B}_p = \mu_0 (\mathbf{J}_f + \mathbf{J}_i), \quad (4)$$

being $\mu_0 \approx 4\pi \times 10^{-7}$ [H/m] the magnetic permeability of free space, and \mathbf{J}_i the so-called induced current [20].

Interpreting \mathbf{J}_i as the outcome of an induced magnetization \mathbf{M}_i allows the following relation to hold:

$$\mathbf{J}_i = \nabla \times \mathbf{M}_i. \quad (5)$$

If we rewrite Eq. (4) in the form

$$\nabla \times \mathbf{B}_p = \mu_0 (\mathbf{J}_f + \nabla \times \mathbf{M}_i), \quad (6)$$

and re-arrange terms, then

$$\nabla \times \left(\frac{1}{\mu_0} \mathbf{B}_p - \mathbf{M}_i \right) = \mathbf{J}_f. \quad (7)$$

To simplify this expression, it is customary to introduce the auxiliary field \mathbf{H} , defined as

$$\mathbf{H} \equiv \frac{1}{\mu_0} \mathbf{B}_p - \mathbf{M}_i + \nabla \phi, \quad (8)$$

being ϕ is an arbitrary scalar field. It is noteworthy that, since the curl of a gradient is identically zero, we are free to choose any ϕ and still satisfy Eq. (7). In particular, choosing $\nabla \phi = 0$ simplifies Equation (8) to

$$\mathbf{H} = \frac{1}{\mu_0} \mathbf{B}_p - \mathbf{M}_i. \quad (9)$$

Then

$$\nabla \times \mathbf{H} = \mathbf{J}_f. \quad (10)$$

For simplicity, we assume a linear the constitutive law [24], so

$$\mathbf{B}_p = \mu \mathbf{H}, \quad (11)$$

being μ the absolute magnetic permeability of the medium. Expanding the equation above using the result from Equation (9) gives

$$\mathbf{B}_p = \mu \left(\frac{1}{\mu_0} \mathbf{B}_p - \mathbf{M}_i \right). \quad (12)$$

From this, we can derive an expression for the magnetization \mathbf{M}_i as a function of the magnetic field as

$$\mathbf{M}_i = \left(\frac{\mu - \mu_0}{\mu \mu_0} \right) \mathbf{B}_p = \chi \mathbf{B}_p, \quad (13)$$

being χ the normalized magnetic susceptibility

$$\chi = \frac{\mu - \mu_0}{\mu \mu_0} = \frac{\mu_r - 1}{\mu_r \mu_0}, \quad (14)$$

and $\mu_r = \mu/\mu_0$ is the relative permeability.

Substituting Equations (10) and (13) into Equation (6), an expanded expression for the Ampere's law in permeable media carrying a free current can be obtained:

$$\nabla \times \mathbf{B}_p = \mu_0 [\nabla \times \mathbf{H} + \nabla \times (\chi \mathbf{B}_p)]. \quad (15)$$

2.2.2. Permanently magnetized media

The distribution of the magnetic field in permanently magnetized media, from now on denoted as \mathbf{B}_m , is governed by the following variant of Ampere's law:

$$\nabla \times \mathbf{B}_m = \mu_0 \mathbf{J}_b. \quad (16)$$

The so-called bound current \mathbf{J}_b is the result of the permanent magnetization; so, both fields relate through [23]

$$\mathbf{J}_b = \nabla \times \mathbf{M}, \quad (17)$$

being \mathbf{M} the magnetization vector. We can expand Equation (16) incorporating Equation (17) to obtain

$$\nabla \times \mathbf{B}_m = \mu_0 \nabla \times \mathbf{M}, \quad (18)$$

which represents the final form of the Ampere's law for magnetized media.

2.2.3. Combined form of the Ampere's law

In systems consisting of both permeable, magnetized and current-carrying bodies, the resulting magnetic field \mathbf{B} comprises contributions from both \mathbf{B}_p and \mathbf{B}_m . Then, Ampere's law yields

$$\nabla \times \mathbf{B} = \nabla \times \mathbf{B}_p + \nabla \times \mathbf{B}_m = \mu_0 (\mathbf{J}_f + \mathbf{J}_i + \mathbf{J}_b). \quad (19)$$

Injecting the expressions for the induced and bound currents we obtain

$$\nabla \times \mathbf{B} = \mu_0 [\mathbf{J}_f + \nabla \times (\chi \mathbf{B}_p) + \nabla \times \mathbf{M}]. \quad (20)$$

Now, after assuming the relative permeability of the magnetized medium satisfies $\mathbf{B}_p = \mathbf{B}$, we can devise the generalized Ampere's law for the entire domain as

$$\nabla \times \mathbf{B} = \mu_0 [\mathbf{J}_f + \nabla \times (\chi \mathbf{B}) + \nabla \times \mathbf{M}]. \quad (21)$$

This equation is valid only if the permeable media is not permanently magnetized and if the magnetized material has relative permeability equal to 1.

2.3. Vector potential formulation

By virtue of Gauss law, the magnetic field is solenoidal; this means it can be expressed as the curl of an auxiliary vector field \mathbf{A} , normally called the magnetic vector potential, such that

$$\mathbf{B} = \nabla \times \mathbf{A}. \quad (22)$$

Choosing Coulomb's gauging, i.e. $\nabla \cdot \mathbf{A} = 0$ [22], allows writing Equation (21) as

$$\nabla^2 \mathbf{A} = -\mu_0 [\mathbf{J}_f + \nabla \times (\chi \mathbf{B}) + \nabla \times \mathbf{M}]. \quad (23)$$

After expanding the curl in the second term in the RHS, the following expression for the vector potential balance equation can be obtained: [20]

$$\nabla^2 \mathbf{A} = \frac{-\mu_0}{1 - \chi \mu_0} [\mathbf{J}_f + (\nabla \chi) \times (\nabla \times \mathbf{A}) + \nabla \times \mathbf{M}]. \quad (24)$$

Although this equation is in its own right a balance law for magnetostatics, its numerical discretization using the FVM leads to non-conservative scheme due to the presence of the second term in the RHS. However, exploiting identities A.6, A.4 and A.5 while defining $\nabla \tilde{\mathbf{A}} = (\nabla \mathbf{A} - \nabla \mathbf{A}^T)$, the following conservative variant can be developed: [20]

$$\nabla^2 \mathbf{A} = -\mu_0 [\mathbf{J}_f - \nabla \cdot (\chi \nabla \tilde{\mathbf{A}}) + \nabla \times \mathbf{M}]. \quad (25)$$

2.4. Interface boundary condition

A crucial aspect of the current formulation is that boundary conditions must be applied to the vector potential at the interfaces between the various media comprising the magnetostatic system to ensure that magnetic field discontinuity is calculated properly. As demonstrated in [20], the vector potential and the normal component of the magnetic field remain continuous across the interface. So, being \mathbf{e}_n the interface unit normal vector, the jumps in the vector potential and in the magnetic field across the interface are

$$\Delta \mathbf{A} = \mathbf{0}, \quad (26)$$

and

$$\Delta \mathbf{B} \cdot \mathbf{e}_n = 0. \quad (27)$$

Conversely, the tangential component of the vector potential experiences a discontinuity at the interface, and thus the magnitude of its jump is

$$\Delta \mathbf{B} = \mu_0 \mathbf{K} \times \mathbf{e}_n, \quad (28)$$

where \mathbf{K} is a generalized surface current defined as

$$\mathbf{K} = -\mathbf{K}_f + \Delta (\chi \mathbf{B} + \mathbf{M}) \times \mathbf{e}_n. \quad (29)$$

Therefore, the existence of this interface current leads to a discontinuity in the tangential component of the magnetic field, which in turn leads to a discontinuity in the normal gradient of the vector potential

of magnitude [20]

$$\frac{\partial \Delta \mathbf{A}}{\partial e_n} = -\mu_0 \mathbf{K}. \quad (30)$$

The equations above provide the relation between of the magnetic field and the vector potential on both sides of interfaces that must be fulfilled in order to satisfy the magnetostatic equilibrium equations.

3. Numerical scheme

3.1. Finite Volume formulation

The primary objective of this paper is to introduce a Finite Volume scheme for the numerical solution of Equation (25) within a magnetostatic system comprised of subsystems consisting of permeable, magnetized, and current-carrying media. The scheme involves dividing each subsystem into a finite set of arbitrarily irregular polyhedral cells. These cells are fixed in space, forming a volume over which each operator of the magnetostatic differential equations and corresponding interface and boundary conditions are discretized. The results of this discretization is a linear system of algebraic equations that are solved in a sequential manner.

We propose to discretize and integrate the balance equations in a region-wise approach. So, for each region encompassing a subsystem we define a control volume V_i and integrate Equation (25) as

$$\int_{V_i} \nabla^2 \mathbf{A} \, dV = -\mu_0 \int_{V_i} \left[\mathbf{J}_f - \nabla \cdot (\chi \nabla \tilde{\mathbf{A}}) + \nabla \times \mathbf{M} \right] \, dV. \quad (31)$$

At the end of the discretization process we obtain n linear systems of equations of the form

$$\mathbf{S}_i \mathbf{A}_i = \mathbf{F}_i, \quad (32)$$

being \mathbf{S}_i the system matrix for region i and \mathbf{F}_i the forcing vector resulting from the explicit discretization of the RHS of Eq. (31) and other explicit terms associated to the interface boundary conditions and non-orthogonal corrections.

We adopt a segregated solution strategy; so each of the subsystems is solved independently and sequentially, and the interaction between them is accounted for by the numerical discretization of the interface boundary conditions.

3.1.1. Laplacian discretization

The Laplacian operator is discretized with the help of Gauss' divergence theorem as

$$\int_{V_i} \nabla^2 \mathbf{A} \, dV = \int_{V_i} \nabla \cdot (\nabla \mathbf{A}) \, dV \approx \sum \mathbf{s}_f \cdot \nabla \mathbf{A}_f, \quad (33)$$

where \mathbf{s}_f is the surface vector, and \mathbf{A}_f is the magnetic vector potential at face f . The last equation can also be written in terms of the surface normal gradient as

$$\sum \mathbf{s}_f \cdot \nabla \mathbf{A}_f = \sum |\mathbf{s}_f| \hat{\mathbf{n}} \cdot \nabla \mathbf{A}_f.$$

The normal gradient of the magnetic vector potential at the faces –or surface normal gradient– is required to evaluate the Laplacian. For orthogonal meshes its numerical evaluation is based on a central difference of cell values on each side of the face,

$$\hat{\mathbf{n}} \cdot \nabla \mathbf{A}_f = \hat{\mathbf{r}} \cdot \nabla \mathbf{A}_f = \frac{\mathbf{A}_C - \mathbf{A}_E}{|\mathbf{r}|}, \quad (34)$$

being \mathbf{r} the relative position vector between centers of cells C and E , which share face f .

This calculation maintains second-order accuracy when the vector connecting the cell centers is orthogonal to the face [25]. However, when structured or unstructured non-orthogonal meshes are employed, the described discretization process loses accuracy since the surface normal vector \mathbf{s}_f and \mathbf{r} are no longer collinear, as illustrated in Figure 1. This implies that, for non-orthogonal meshes,

$\hat{\mathbf{n}} \cdot \nabla \mathbf{A}_f \neq \hat{\mathbf{r}} \cdot \nabla \mathbf{A}_f$. As Equation (34) yields $\hat{\mathbf{r}} \cdot \nabla \mathbf{A}_f$, and to evaluate the Laplacian we require computing $\hat{\mathbf{n}} \cdot \nabla \mathbf{A}_f$, an alternative scheme must be employed.

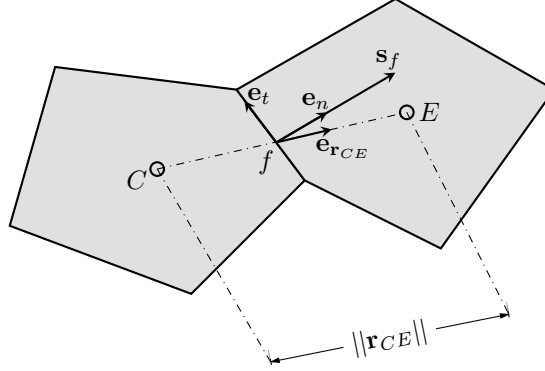


Figure 1: Depiction of neighboring elements in a non-orthogonal mesh.

Although it is not possible to calculate the face normal gradient implicitly, we can calculate the full gradient of the magnetic vector potential at the cell center explicitly as

$$\overline{\nabla \mathbf{A}_C} = \frac{1}{V} \sum \mathbf{s}_f \cdot \mathbf{A}_f. \quad (35)$$

This expression allows finding the face gradient explicitly using linear interpolation in the form

$$\overline{\nabla \mathbf{A}_f} = w \nabla \mathbf{A}_C + (1 - w) \nabla \mathbf{A}_E, \quad (36)$$

being w an interpolation factor, and the overbar denotes values that are calculated explicitly.

Now, we split the evaluation of the face gradient in a orthogonal component $\nabla \mathbf{A}_f^o$ and a non-orthogonal component $\nabla \mathbf{A}_f^n$ as

$$\nabla \mathbf{A}_f = \nabla \mathbf{A}_f^o + \nabla \mathbf{A}_f^n. \quad (37)$$

We can then extract the normal direction of each gradient to obtain

$$\hat{\mathbf{n}} \cdot \nabla \mathbf{A}_f = \hat{\mathbf{n}} \cdot \nabla \mathbf{A}_f^o + \hat{\mathbf{n}} \cdot \nabla \mathbf{A}_f^n. \quad (38)$$

Next, we can approximate both the orthogonal component and the LHS of Eq. (38) using the explicit gradient in Eq. (36) as $\hat{\mathbf{n}} \cdot \nabla \mathbf{A}_f^o \simeq \hat{\mathbf{r}} \cdot \overline{\nabla \mathbf{A}_f}$ and $\hat{\mathbf{n}} \cdot \nabla \mathbf{A}_f \simeq \hat{\mathbf{n}} \cdot \overline{\nabla \mathbf{A}_f}$. Therefore, we can approximate the non-orthogonal component of the face normal gradient in Eq. (36) explicitly as

$$\hat{\mathbf{n}} \cdot \overline{\nabla \mathbf{A}_f^n} = (\hat{\mathbf{n}} - \hat{\mathbf{r}}) \cdot \overline{\nabla \mathbf{A}_f}. \quad (39)$$

Finally, injecting Eqs. (39) and (34) into Eq. (38) allows us to find an implicit-explicit expression for the face normal gradient of the magnetic vector potential, namely

$$\hat{\mathbf{n}} \cdot \nabla \mathbf{A}_f = \frac{\mathbf{A}_C - \mathbf{A}_E}{|\mathbf{r}|} + (\hat{\mathbf{n}} - \hat{\mathbf{r}}) \cdot \overline{\nabla \mathbf{A}_f}.$$

This expression must be iterated until convergence in a loop that, in the context of fluid mechanics, is often called non-orthogonal correction.

3.1.2. Induced and bound current discretization

The second term in the RHS of Equation (31) is calculated explicitly using a Gauss scheme; this yields

$$\int_{V_i} \nabla \cdot (\chi \nabla \tilde{\mathbf{A}}) dV_i \approx \sum \chi_f \mathbf{s}_f \cdot \nabla \tilde{\mathbf{A}}_f, \quad (40)$$

where χ_f is the magnetic susceptibility at face f . The susceptibility at internal faces is calculated using linear interpolation as

$$\chi_f = (1 - w) \chi_C + w \chi_E, \quad (41)$$

being $w = |\mathbf{r}_{Cf}|/|\mathbf{r}_{Ec}|$ the interpolation factor.

At interface faces, the material susceptibility is likely to have discrete jumps; using interpolation at this faces would smear the susceptibility field unrealistically. Therefore, we evaluate the face susceptibility as

$$\chi_f = \chi_C + \mathbf{r}_{Cf} \cdot \nabla \chi_C, \quad (42)$$

for which the susceptibility cell gradient is evaluated explicitly using a Gauss scheme,

$$\nabla \chi_C = \frac{1}{V_C} \sum \chi_f \mathbf{s}_f. \quad (43)$$

To complete the derivation of the discretization scheme, we discretize the bound current explicitly using the Hodge dual ${}^*()$; this yields

$$\int_{V_i} \nabla \times \mathbf{M} \, dV \approx 2^* \left(\nabla \widetilde{\mathbf{M}}_C \right). \quad (44)$$

This method allows choosing a convenient scheme for the gradient of the magnetization.

3.2. Solution scheme

The numerical discretization presented in the last section results in coupled sets of nonlinear algebraic equations involving variables corresponding to different media. In order to solve this multi-domain problem, we can opt for a monolithic or a partitioned approach. The monolithic or direct approach addresses all domains simultaneously, solving a single set of algebraic equations encompassing all relevant variables. On the other hand, the partitioned or segregated approach solves the system of equation of each domain individually and sequentially, treating the coupling terms associated to the interactions between regions explicitly [26, 27].

The monolithic approach generates variables that exhibit heterogeneity as they represent discretization across diverse domains; thus, scalability, parallelism, preconditioning and performance are commonly an issue [27]. The monolithic solution of Eq. (31) with the embedded discontinuity interface conditions in Eq. (30) poses a question about stability issues in strongly coupled problems.

In a segregated multi-region scheme solving of a large system is avoided at the expense of iterations between smaller systems; typically, the main concerns are stability and implementation [28]. Also, field transfer between domains, convergence acceleration and synchronization of region solutions are numerical and computational difficulties that must be addressed. However, we argue that the partitioned approach is still more appealing because existing field operation libraries, such as OpenFOAM [29], are equipped with several discretization, mapping and convergence checking algorithms that can be straightforwardly combined to develop an effective segregated solver. In this paper, this is the approach we adopt.

The solution scheme we propose is as follows: suppose a two-region magnetic system, then the system matrix corresponding to the discretized version of Eq. (25) is

$$\begin{bmatrix} \mathbf{L}_{11} + \mathbf{N}_{11}(\mathbf{A}_1) & \mathbf{N}_{12}(\mathbf{A}_2) \\ \mathbf{N}_{21}(\mathbf{A}_1) & \mathbf{L}_{22} + \mathbf{N}_{22}(\mathbf{A}_2) \end{bmatrix} \begin{bmatrix} \mathbf{A}_1 \\ \mathbf{A}_2 \end{bmatrix} = \begin{bmatrix} \mathbf{F}_1 \\ \mathbf{F}_2 \end{bmatrix}, \quad (45)$$

being \mathbf{L}_{jj} are linear operators, \mathbf{N}_{jj} are nonlinear operators, \mathbf{A}_1 and \mathbf{A}_2 are the vector potentials for each region, and \mathbf{F}_1 and \mathbf{F}_2 correspond to the explicit discretization of the RHS of Eq. (25).

A direct solution of Eq. (45) can be obtained using linearization schemes available for the solution of nonlinear problems, such as the Newton–Raphson method, the Picard method, etc. Instead, we choose to use a block iterative scheme of the form

$$\mathbf{L}_{11} \mathbf{A}_1^i = \mathbf{F}_1 - \mathbf{N}_{11}(\mathbf{A}_1^{i-1}) \mathbf{A}_1^{i-1} - \mathbf{N}_{12}(\mathbf{A}_2^{i-1}) \mathbf{A}_2^{i-1}, \quad (46)$$

and

$$\mathbf{L}_{22}\mathbf{A}_2^i = \mathbf{F}_2 - \mathbf{N}_{22}(\mathbf{A}_2^{i-1})\mathbf{A}_2^{i-1} - \mathbf{N}_{21}(\mathbf{A}_1^i)\mathbf{A}_1^i, \quad (47)$$

where i is the iteration counter index. The use of the last available solution for region 1 in the last term in the RHS of Eq. (47) indicates that this iteration loop is a block Gauss–Seidel scheme (BGS).

This algorithm is effective for solving the coupled multi–region systems; however, the convergence is greatly affected by the sequential nature of the solver. With highly non–orthogonal or skewed grids and ill conditioned systems, large variations in \mathbf{A} occur during the solution process, which can cause loss of convergence. To promote convergence and stabilize the iterative process, a practical approach is to under–relax certain fields between iterations.

Because the RHS of a region’s system is a function of second derivatives of \mathbf{A} , relaxing \mathbf{A} does not always stabilize the solution. It is not uncommon to find that for cases involving highly permeable materials the solution diverges. Also, as Eq. 30 shows, the interface boundary condition is a function of a jump in the magnetic field at both sides of the interface. Since the BGS scheme solves each region at a time, during the region sequential loop, one of the interface neighboring cell center values is updated, while the others do not. This often generates large oscillations in the interface jumps.

In the numerical implementation, the interface boundary condition feeds the Laplacian operator with the face normal gradient of the vector potential,

$$\frac{\partial \mathbf{A}_e^C}{\partial e_n} = a_C \mathbf{A}^C + a_E \mathbf{A}^E + a_K \mathbf{K}, \quad (48)$$

being a_C the gradient internal factor and a_E and a_K gradient boundary factors [25] and the generalized surface current given by 29.

Since the free surface current \mathbf{K}_f and the permanent magnetization \mathbf{M} are generally constant and uniformly distributed, the oscillation of the surface current is generated by $\Delta(\chi\mathbf{B})$; this suggests that its relaxation would certainly help convergence. The first term in the RHS of Eq. (48) adds to the diagonal of the system matrix, while the other two add to the RHS. For the case of interface faces, the second term is not a matrix term because the neighboring cell center value belongs in a different region. In regards to the third term, it must be evaluated explicitly because the interface current cannot be written in terms of \mathbf{A}^C since the curl couples the vector components. Therefore, both the second and third terms may generate sharp changes in the RHS of the region system, leading to instabilities in poor conditioned systems.

In the same direction, the divergence term in the RHS of Eq. (25) is discretized explicitly as given by Equation 40; implicit integration is not possible since the skew operator couples the vector components of the vector potential. In this circumstances, the vector potential gradient can generate values with an nonphysically large magnitude in highly non–orthogonal meshes. A large gradient value in one cell can contribute sufficiently to the source term of an equation to cause unboundedness in the solution.

In order to alleviate the mentioned issues, we use field relaxation. The main objective of implementing relaxation is to slow down the changes of the solution variable during the iteration process, which helps to avoid divergence due to mesh non–orthogonality.

Experimental findings suggest that both implicit and explicit relaxation can improve the convergence of the proposed solver. For the case of explicit relaxation, a field ϕ in the current iteration is evaluated in terms of the actual solution of the region system ϕ_c , and the previous iteration solution ϕ_o as [25]

$$\phi = \phi_o + \lambda(\phi_c - \phi_o), \quad (49)$$

where λ represents the relaxation factor.

As it can be seen from the expression above, the current field ϕ is not the calculated ϕ_c but a fraction of it, this reduces oscillations for values of $\lambda < 1$. When convergence is reached, the correction tends to zero and $\phi_c = \phi_o$. Although reducing the value of λ increases stability, the correction is also reduced and the convergence is slowed down.

Our experimental findings show that when explicit relaxation is used, the proposed iterative block

algorithm diverges for most high permeability configurations. Under this circumstances, the following implicit relaxation strategy has shown to improve stability.

Consider the matrix equation

$$\mathbf{C}\phi = \mathbf{D}, \quad (50)$$

being \mathbf{C} a coefficients matrix of size $n \times n$, ϕ the solution vector and \mathbf{D} a source term. For a single cell P , the equation is

$$C_{P1}\phi_1 + C_{P2}\phi_2 + \dots + C_{P(P-1)}\phi_{P-1} + C_{PP}\phi_P + C_{P(P+1)}\phi_{P+1} + \dots + C_{Pn}\phi_n = D_P. \quad (51)$$

Since we want the solution for cell P , i.e. ϕ_P , we can collect the other terms together, which, using summation notation, gives

$$C_P\phi_P + \sum_{nb} C_{nb}\phi_{nb} = D_P, \quad (52)$$

where nb stands for neighbor cells. Thus, we can express the solution for cell P in the form

$$\phi_P = \frac{1}{C_P} \left(- \sum_{nb} C_{nb}\phi_{nb} + D_P \right). \quad (53)$$

This value corresponds to the component P of ϕ . Now, explicitly relaxing ϕ_P

$$\phi_P = \phi_o + \lambda \left[\frac{1}{C_P} \left(- \sum_{nb} C_{nb}\phi_{nb} + D_P \right) - \phi_o \right]. \quad (54)$$

Multiplying both sides by C_P/λ and rearranging terms results in

$$\frac{C_P}{\lambda} \phi_P + \sum_{nb} C_{nb}\phi_{nb} = D_P + \left(\frac{1-\lambda}{\lambda} \right) C_P \phi_o. \quad (55)$$

Writing Equation 55 in matrix form yields

$$\begin{bmatrix} \frac{C_{11}}{\lambda} & \dots & C_{1n} \\ \vdots & \ddots & \vdots \\ C_{n1} & \dots & \frac{C_{nn}}{\lambda} \end{bmatrix} \begin{bmatrix} \phi_1 \\ \vdots \\ \phi_n \end{bmatrix} = \begin{bmatrix} D_1 + \left(\frac{1-\lambda}{\lambda} \right) C_{11} \phi_{1,o} \\ \vdots \\ D_n + \left(\frac{1-\lambda}{\lambda} \right) C_{nn} \phi_{n,o} \end{bmatrix}. \quad (56)$$

From the equation above, it is clear that implicit relaxation enhances the diagonal dominance of the system matrix, i.e. each cell's contribution to its own solution becomes more significant compared to the influence of neighboring cells. The increased diagonal dominance promotes stability, as it ensures smoother propagation of changes throughout the system, thereby reducing the likelihood of oscillations or divergence during the iterative process. Another consequence of implicit relaxation is an increase in the source term, which typically slows down convergence.

At this point, it is important to remark that there are two primary strategies for implementing under-relaxation at the multi-region solver level. The first involves a region-wise application, while the second applies simultaneous relaxation to all regions. The former approach introduces a significant dependency on the order in which regions are solved, as an under-relaxed solution may propagate to neighboring regions through the interface boundary conditions. Conversely, such concerns are mitigated in the latter approach, as the relaxation of the right-hand side of the equilibrium equation is uniformly applied across all regions before commencing the iterative solution loop.

4. Numerical experiments

In this section, we present an assessment of the method's performance. We evaluate its capability to accurately capture discontinuous distributions of magnetic fields in configurations comprising permeable, permanently magnetized, and current-carrying media by comparing its results with those obtained using the Finite Element Method. All test cases are two-dimensional and are constructed using triangular non-structured meshes.

4.1. Magnetized and permeable media interaction - Case 1

The first test consists of a squared magnet interacting with a permeable material. As Figure 2 shows, the configuration consists of a cylindrical shaped permeable material, called *ferro*, with diameter $\phi = 0.075$ m and a squared permanently magnetized material, called *magnet*, with sides of length 0.1 m. The ferro's relative permeability is $\mu_r = 30$ and the permanent magnetization of the magnet is $\mathbf{M} = 9.75 \times 10^5 \text{ A m}^{-1} \mathbf{e}_y$; being \mathbf{e}_y the unit vector pointing to vertical direction. Both the magnet and the ferro are immersed in an air volume of dimensions 1 m \times 1 m \times 1 m. Air magnetic properties are assumed to be $\mu_r = 1$ and $\mathbf{M} = 0$. At the outer boundaries of the air volume we specify the boundary condition $\mathbf{A} = 0$; while at all interfaces we specify the boundary condition in Eq. (48).

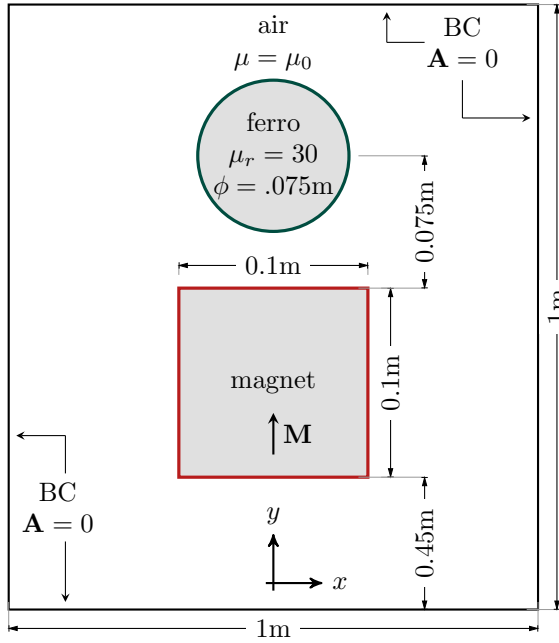


Figure 2: Schematic of benchmark Case 1.

The mesh density around the ferro and magnet has fixed edge size of 5×10^{-3} m; Figure 3 shows the mesh.

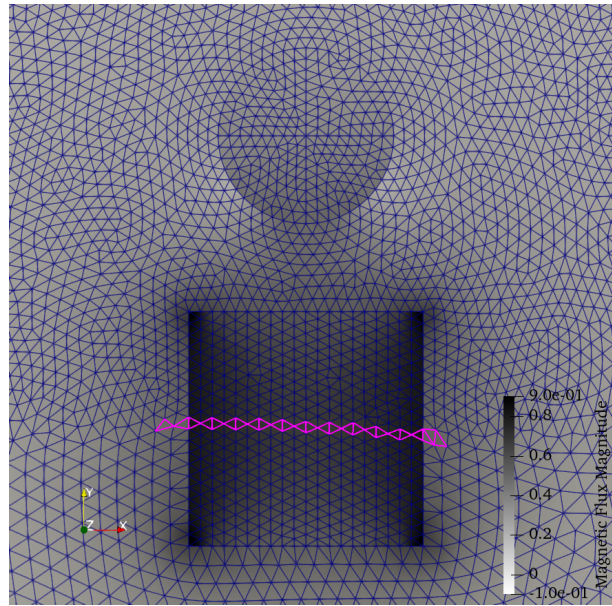


Figure 3: Benchmark Case 1 mesh.

Figures 4 and 5 show the surface line integral convolution (SLIC) of the magnetic field obtained with

the present formulation and the FEM. From a qualitative viewpoint, it is clear that both approaches agree very well. The discontinuities of the tangential component of the magnetic at the interfaces between both the magnet and the permeable material and air between different media are very similarly captured by both approaches.

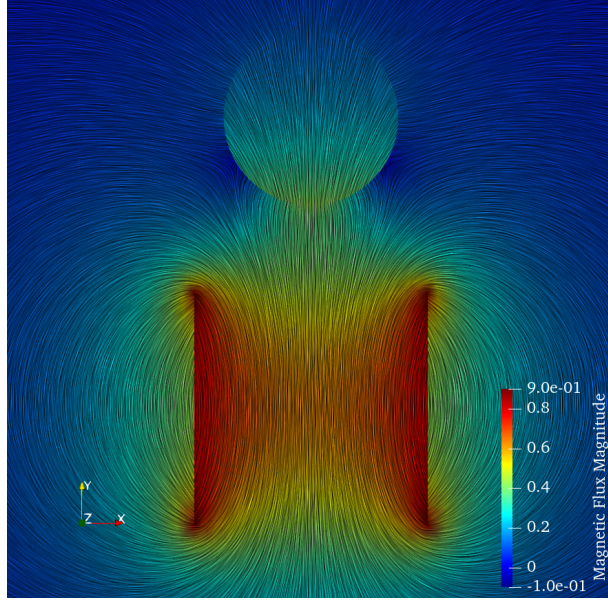


Figure 4: Magnetic field SLIC for Case 1 – FEM solution.

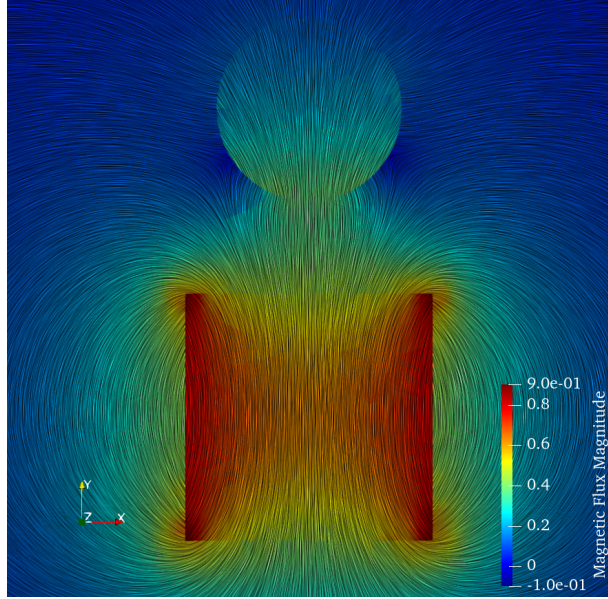


Figure 5: Magnetic field SLIC for Case 1 – Present FVM solution.

Figure 6 shows the change in the y -component of the magnetic field at the cell centroids through the arbitrary path shown in Figure 3. It is important to note that since the Finite Element formulation gives magnetic field values at the element edges, in order to compare the results against the present cell-centered FVM, it was necessary to interpolate the FEM data to the element centroid. As it can be seen, the formulation is able to capture correctly the discontinuous distribution of the magnetic field.

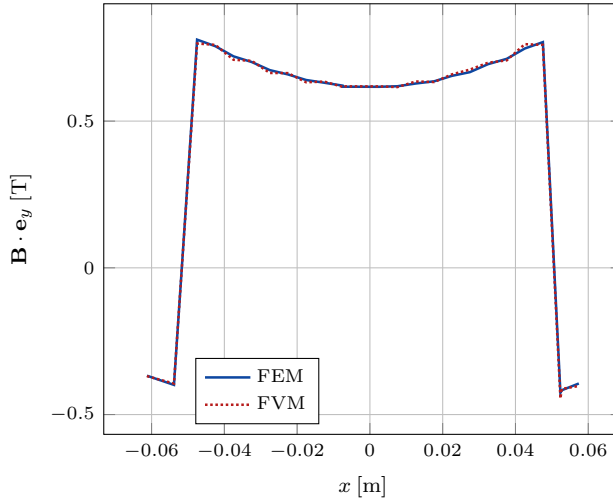


Figure 6: Vertical component of the magnetic field.

4.2. Magnetized and permeable media interaction - Case 2

Expanding upon the initial comparison, we tested the FV method with the configuration shown in Figure 7, which features a domain composed of both cylindrical shaped magnet and permeable materials, with diameters $\phi = 0.1\text{ m}$ and $\phi = 0.075\text{ m}$ respectively. The magnetization is kept as $\mathbf{M} = 9.75 \times 10^5 \text{ A m}^{-1} \mathbf{e}_y$.

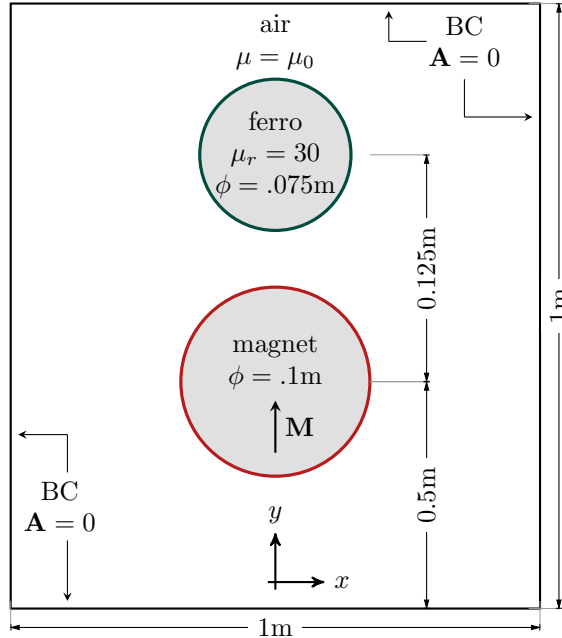


Figure 7: Schematic of benchmark Case 2.

The results of the numerical experiment are shown in Figure 8. Qualitatively, the discontinuities in direction and magnitude of \mathbf{B} arising at the interfaces are captured correctly by the solver. Then, far from the ferro-air and magnet-air interfaces, the results are consistent with [20] and [21] and the FEM edge prediction shown in the previous section.

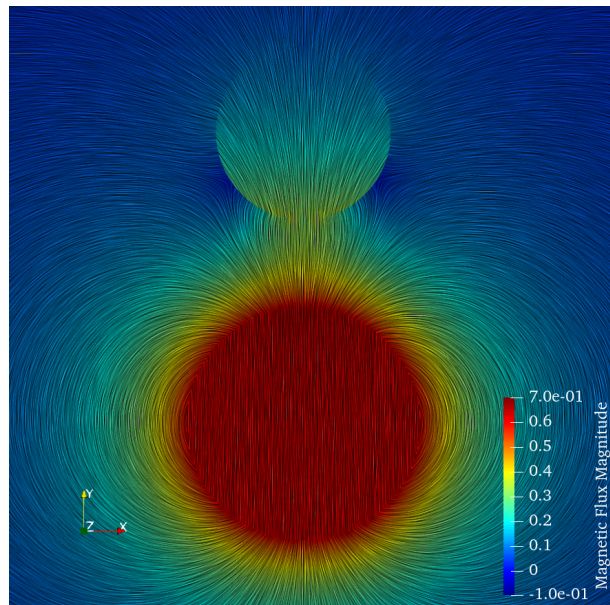


Figure 8: Magnetic field SLIC.

This agreement is confirmed by the quantitative analysis presented in Figure 9, where the variation in the y -component of the magnetic field is plotted along a vertical path through the center of the domain.

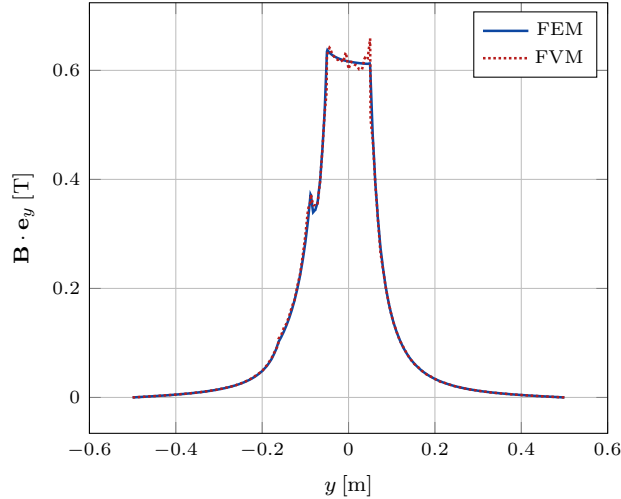


Figure 9: Vertical component of the magnetic field.

4.3. Magnetized, permeable and volumetric current media interaction - Case 3

Next, we assess the method's behavior in a case with strong interaction among three curved materials. The configuration is shown in Figure 10, with the benchmark test being composed of a magnet and ferro materials with the same physical characteristics as in Cases 1 and 2, and additionally a current carrying media of diameter $\phi = 0.075$ m and current vector $\mathbf{J} = 2.5 \times 10^7 \text{ A m}^{-2} \mathbf{e}_z$.

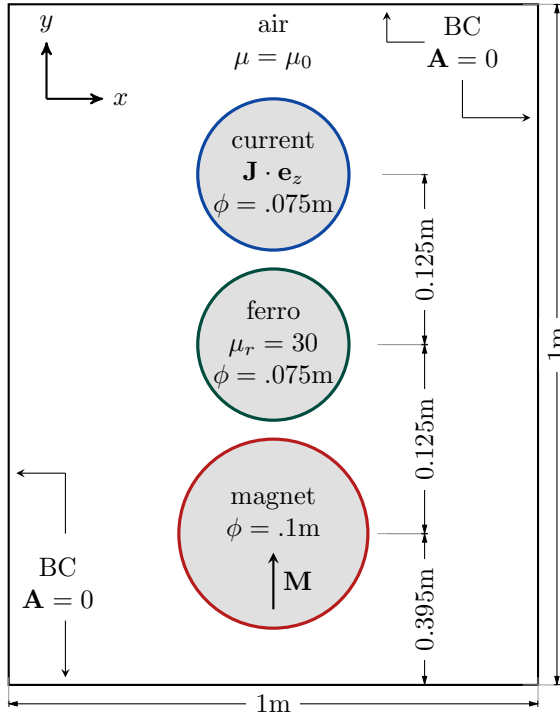


Figure 10: Benchmark test schematic.

The resulting magnetic field may be observed in Figure 11. The current carrying material is characterized by the lack of surface currents \mathbf{K}_f , and thus the RHS of the boundary condition, Eq. 30, is null since $\Delta\chi\mathbf{B} = \Delta\mathbf{M}$. Accordingly, the normal and tangential components of the vector potential in the interface of the current material are continuous. As it can be seen qualitatively in the figure, the method is able to capture the changes in the direction and magnitude of the vector magnetic field in all three materials.

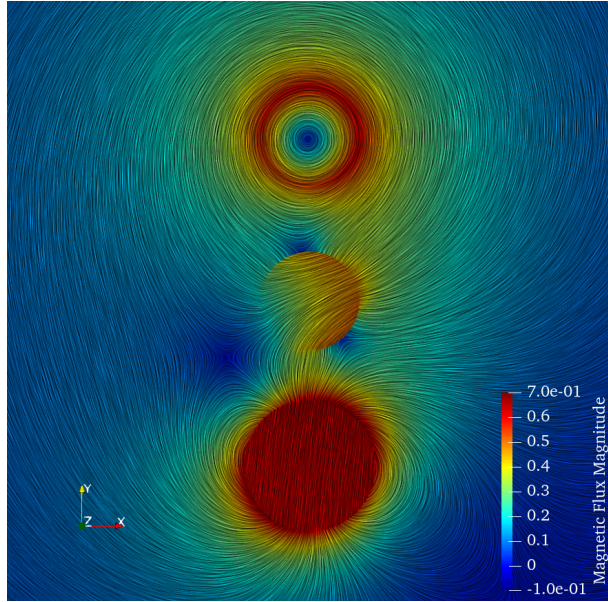


Figure 11: Magnetic field SLIC.

Quantitatively, the results are illustrated in Figure 12. In this case, the changes in the x - and y -components of the magnetic field, as well as the change in the z -component of the magnetic vector potential, are plotted. The method successfully captures the variations in the magnetic field despite the strong interactions between the media. Notably, the plot of the magnetic vector potential closely aligns

with the FEM results; whereas the magnetic field plots exhibit more error due to the additional step of taking the curl of the solution \mathbf{A} .

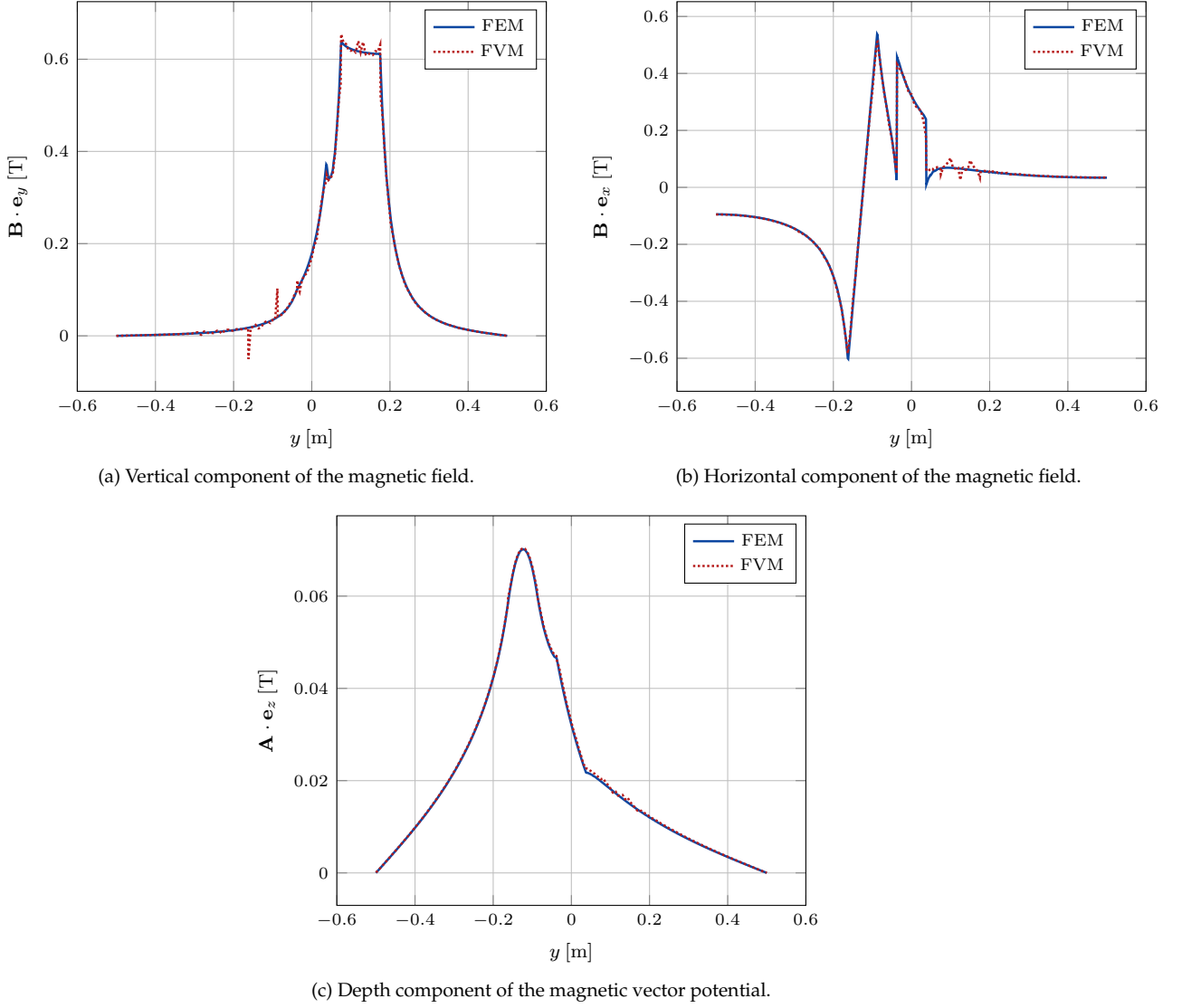


Figure 12: Quantitative assessment of Case 3.

4.4. Non-orthogonality test - Case 4

Finally, we solve the configuration depicted in Figure 13, which is taken from [20, 21]. The objective of this test is to compare the results obtained with orthogonal and non-orthogonal meshes. The configuration consists of two squared materials: a magnet of sides 0.1 m and a ferro of size 0.1 m \times 0.05 m, surrounded by a volume of air of dimensions 1 m \times 1 m.

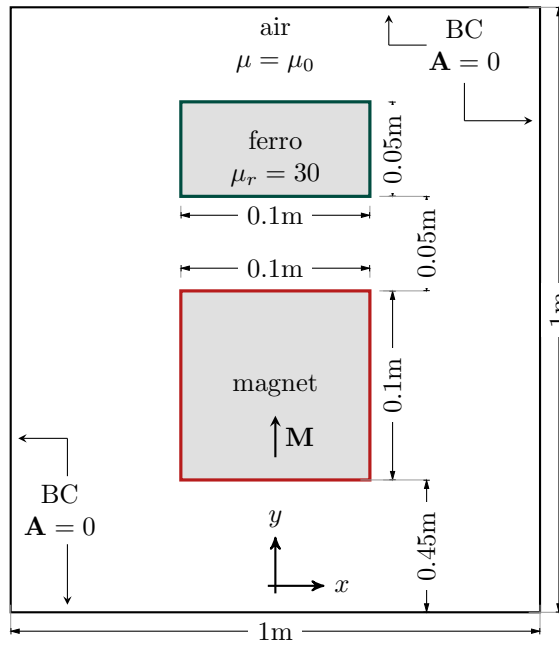


Figure 13: Case 4 schematic.

The results of this test are shown in Figure 14, while Figure 15 depicts the same results but with an orthogonal and uniform mesh, maintaining similar mesh density. As it can be seen from the qualitative assessment, the calculation of the magnetic field coincides regardless of the mesh. However, in the non-orthogonal case, convergence is only achieved taking into account considerations such as field relaxation. This is not case for the orthogonal experiment, where these considerations are not necessary and therefore not implemented.

The results of this test are presented in Figure 14 and 15. The figures show the magnetic field distribution obtained with non-orthogonal and orthogonal meshes, respectively. Both meshes have comparable density. The qualitative assessment indicates that regardless of the mesh topology, the algorithm is able to predict the same magnetic field. A key point is that the convergence of the non-orthogonal case requires the use of a relaxation technique. In this case, we have used implicit relaxation with a relaxation factor $\lambda = 0.8$; larger values of λ cause divergence.

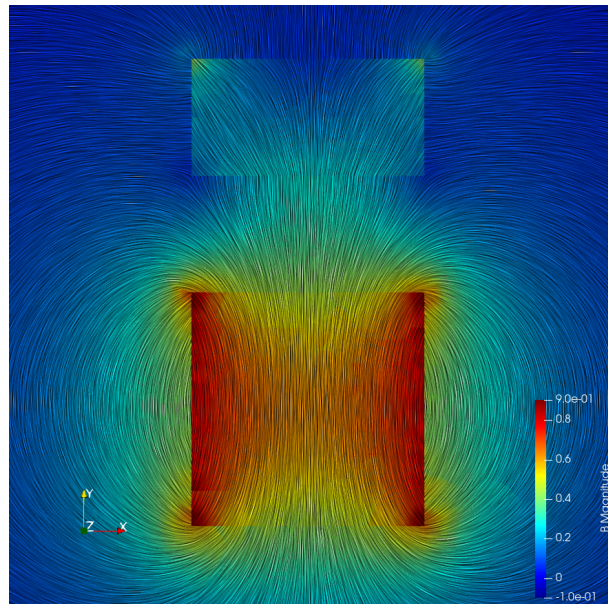


Figure 14: Magnetic field SLIC – Non-orthogonal mesh.

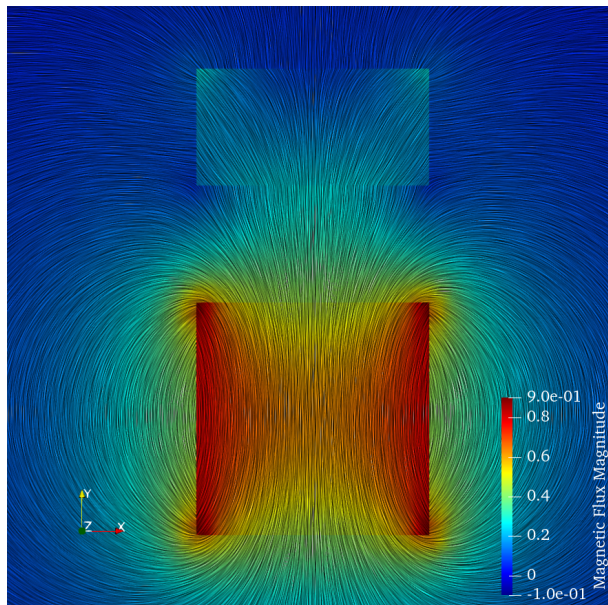


Figure 15: Magnetic field SLIC – Orthogonal mesh.

As a general observation, we note that behavior of both Gauss-linear and least-squares gradient methods for the evaluation of the non-orthogonal face normal gradient in Eq. (39) were evaluated. It was found that the least-squares gradient typically yields divergent solutions, whereas the Gauss gradient method consistently demonstrates stability.

Numerical experiments also indicate that convergence is governed by the bound current term $\nabla \cdot (\chi \nabla \tilde{\mathbf{A}})$. Convergence is often guaranteed by under-relaxing this term with $\lambda \approx 0.8$. The relaxation of the magnetic vector potential and/or the magnetic field does not seem to help convergence. Comparisons between implicit and explicit relaxation schemes reveal that implicit relaxation is generally more efficient, resulting in higher relaxation factors and faster solutions.

We have also tested the χ scaling approach suggested in [20] for the improving the convergence behavior in orthogonal meshes. This approach does not improve the convergence behavior in non-orthogonal meshes.

5. Conclusions and future work

We presented an analysis of discontinuous distributions of magnetic field within curved media discretized with non-orthogonal grids. A formulation where the balance equation is based upon the magnetic vector potential has been developed and tested in diverse numerical settings with non-orthogonal meshes. Since the interface vector magnetic potential is provided by the solution rather than being enforced as an internal boundary condition, numerical experiments have been developed to asses the magnetic field in the multi-media interface.

One of the key conclusions that have been reached from the numerical experiments is the considerations neccesary to achieve convergence with non-orthogonal grids. We have ascertained that field relaxation is imperative in order to find a solution; precisely, relaxing the divergence term in the RHS of Equation 25 with a factor $\lambda \sim \mathcal{O}(0.8)$ is needed instead of scaling the parameter χ as it has been done in [20] for orthogonal meshes. This has been verified by comparing the cell centre values of the Finite Volume framework with interpolated values given by the FE COMSOL solver.

Once the predictions were verified and contrasted against the FE solver, further numerical experiments have been benchmarked in order to test the approach in more complex geometries and with stronger field interactions. The results suggest that the solver is capable of handling these geometries, finding solutions regardless of the meshing techniques employed to discretize the space.

The effects of non-orthogonality have been assessed numerically by comparing the surface line integral convolution plots with both triangular and quadratic conformal grids within the same geometry. Although this comparison is qualitative rather than quantitative, it is useful to get a general idea of the solver's accuracy with non-orthogonal meshes.

The approach has proven to be effective for the computation of discontinuous distributions of magnetic field within curved surfaces. Moreover, the convergence requirements that have been found lay the foundation for more robust computations of magnetic fields. Thus, it is concluded that using a FV scheme shall yield the similar results as a FE solver regardless of the mesh employed.

Appendix A. Vector identities

Being, c a scalar, \underline{a} and \underline{b} vectors, \underline{e}_n a normal unit vector, \underline{T} a tensor, the following identities hold

$$\nabla \times (\nabla \times \mathbf{a}) = \nabla (\nabla \cdot \mathbf{a}) - \nabla^2 \mathbf{a}; \quad (\text{A.1})$$

$$\nabla \times (c \mathbf{a}) = c \nabla \times \mathbf{a} + \nabla c \times \mathbf{a}; \quad (\text{A.2})$$

$$\nabla \cdot (\phi \mathbf{T}) = \phi \nabla \cdot \mathbf{T} + \mathbf{T}^T \nabla \phi \quad (\text{A.3})$$

$$\nabla \cdot (\nabla \mathbf{a}) = \nabla^2 \mathbf{a}; \quad (\text{A.4})$$

$$\nabla \cdot ((\nabla \mathbf{a})^T) = \nabla (\nabla \cdot \mathbf{a}); \quad (\text{A.5})$$

$$(\nabla c) \times (\nabla \times \mathbf{a}) = (\nabla \mathbf{a} - \nabla \mathbf{a}^T) \nabla c. \quad (\text{A.6})$$

Acknowledgments

We would like to thank the support from Consejo Nacional de Investigaciones Científicas y Técnicas and Universidad Tecnológica Nacional through grant PID-ENUTIBB0007877TC.

References

- [1] J. C. Maxwell, Viii. a dynamical theory of the electromagnetic field, *Philosophical transactions of the Royal Society of London* (155) (1865) 459–512.
- [2] C. W. Steele, *Numerical computation of electric and magnetic fields*, Springer Science & Business Media, 2012.
- [3] J. Sykulski, *Computational magnetics*, Springer Science & Business Media, 2012.
- [4] D. A. Lowther, P. P. Sylvester, *Computer-aided design in magnetics*, Springer Science & Business Media, 2012.
- [5] S. Salon, M. Chari, *Numerical methods in electromagnetism*, Elsevier, 1999.
- [6] K. Niu, P. Li, Z. Huang, L. J. Jiang, H. Bagci, Numerical methods for electromagnetic modeling of graphene: A review, *IEEE Journal on Multiscale and Multiphysics Computational Techniques* 5 (2020) 44–58.
- [7] J. R. Cardoso, *Electromagnetics through the finite element method: A simplified approach using maxwell's equations*, Crc Press, 2016.
- [8] J. Coggan, Electromagnetic and electrical modeling by the finite element method, *Geophysics* 36 (1) (1971) 132–155.
- [9] M. N. Sadiku, A simple introduction to finite element analysis of electromagnetic problems, *IEEE Transactions on education* 32 (2) (1989) 85–93.
- [10] M. N. Sadiku, *Numerical techniques in electromagnetics with MATLAB*, CRC press, 2018.
- [11] J.-M. Jin, *The finite element method in electromagnetics*, John Wiley & Sons, 2015.
- [12] A. C. Polycarpou, *Introduction to the finite element method in electromagnetics*, Springer Nature, 2022.
- [13] M. Augustyniak, Z. Usarek, Finite element method applied in electromagnetic ndte: A review, *Journal of Nondestructive Evaluation* 35 (2016) 1–15.
- [14] C.-D. Munz, R. Schneider, U. Voß, A finite-volume method for the maxwell equations in the time domain, *SIAM Journal on Scientific Computing* 22 (2) (2000) 449–475.
- [15] T. S. Chung, J. Zou, A finite volume method for maxwell's equations with discontinuous physical coefficients, *International Journal of Applied Mathematics* 7 (2) (2001) 201–224.
- [16] Y. Liu, M. Vinokur, Z. J. Wang, Spectral (finite) volume method for conservation laws on unstructured grids v: Extension to three-dimensional systems, *Journal of Computational Physics* 212 (2) (2006) 454–472.

- [17] X. Ferrieres, J.-P. Parmantier, S. Bertuol, A. R. Ruddle, Application of a hybrid finite difference/finite volume method to solve an automotive emc problem, *IEEE Transactions on Electromagnetic Compatibility* 46 (4) (2004) 624–634.
- [18] E. Haber, L. Ruthotto, A multiscale finite volume method for maxwell’s equations at low frequencies, *Geophysical Journal International* 199 (2) (2014) 1268–1277.
- [19] L. A. Caudillo-Mata, E. Haber, C. Schwarzbach, An oversampling technique for the multiscale finite volume method to simulate electromagnetic responses in the frequency domain, *Computational Geosciences* 21 (2017) 963–980.
- [20] M. Saravia, A finite volume formulation for magnetostatics of discontinuous media within a multi-region openfoam framework, *Journal of Computational Physics* 433 (2021) 110089.
- [21] A. Riedinger, M. Saravia, A single-region finite volume framework for modeling discontinuous magnetic field distributions, *Computers & Structures* 277 (2023) 106960.
- [22] J. D. Jackson, *Classical electrodynamics* (1999).
- [23] D. J. Griffiths, *Introduction to electrodynamics* fourth edition (2021).
- [24] A. Sommerfeld, *Electrodynamics: lectures on theoretical physics*, vol. 3, Vol. 3, Academic Press, 2013.
- [25] F. Moukalled, L. Mangani, M. Darwish, F. Moukalled, L. Mangani, M. Darwish, *The finite volume method*, Springer, 2016.
- [26] M. Mehl, B. Uekermann, H. Bijl, D. Blom, B. Gatzhammer, A. Van Zuijlen, Parallel coupling numerics for partitioned fluid-structure interaction simulations, *Computers & Mathematics with Applications* 71 (4) (2016) 869–891.
- [27] M. Heil, A. L. Hazel, J. Boyle, Solvers for large-displacement fluid–structure interaction problems: segregated versus monolithic approaches, *Computational Mechanics* 43 (2008) 91–101.
- [28] J. Degroote, S. Anerel, J. Vierendeels, Stability analysis of gauss–seidel iterations in a partitioned simulation of fluid–structure interaction, *Computers & structures* 88 (5-6) (2010) 263–271.
- [29] H. G. Weller, G. Tabor, H. Jasak, C. Fureby, A tensorial approach to computational continuum mechanics using object-oriented techniques, *Computers in physics* 12 (6) (1998) 620–631.